Chinese Chemical Letters 36 (2025) 110501

Contents lists available at ScienceDirect

Chinese Chemical Letters

journal homepage: www.elsevier.com/locate/cclet

Engineered iron-based metal-organic frameworks nanoplatforms for cancer theranostics: A mini review

Yunlong Li[a], Xinyu Zhang[a], Shuang Liu[a], Chunsheng Li[a], Qiang Wang[a], Jin Ye[a], Yong Lu[a,c], Jiating Xu[a,b,*]

[a] Key Laboratory of Forest Plant Ecology, Ministry of Education, College of Chemistry, Chemical Engineering and Resource Utilization, Northeast Forestry University, Harbin 150040, China
[b] Heilongjiang Provincial Key Laboratory of Ecological Utilization of Forestry-Based Active Substances, Northeast Forestry University, Harbin 150040, China
[c] School of Laboratory Medicine, Wannan Medical College, Wuhu 241002, China

ARTICLE INFO

Article history:
Received 30 July 2024
Revised 23 September 2024
Accepted 24 September 2024
Available online 25 September 2024

Keywords:
Bioimaging
Cancer theranostics
Catalytic therapy
Engineered nanoplatforms
Fe-based MOFs

ABSTRACT

Up to now, numerous emerging methods of cancer treatment including chemodynamic therapy, photothermal therapy, photodynamic therapy, sonodynamic therapy, immunotherapy and chemotherapy have rapidly entered a new stage of development. However, the single treatment mode is often constrained by the complex tumor microenvironment. Recently, the nanomaterials and nanomedicine have emerged as promising avenues to overcome the limitation in cancer theranostics. Especially, metal-organic frameworks (MOFs) have gained considerable interests in cancer therapy because of their customizable morphologies, easy functionalization, large specific surface area, and good biocompatibility. Among these MOFs, iron-based MOFs (Fe-MOFs) are particularly promising for cancer treatment due to their properties as nano-photosensitizers, peroxidase-like activity, bioimaging contrast capabilities, and biodegradability. Utilizing their structural regularity and synthetic tunability, Fe-MOFs can be engineered to incorporate organic molecules or other inorganic nanoparticles, thereby creating multifunctional nanoplatforms for single or combined theranostic modes. Herein, the minireview focuses on the recent advancements of the Fe-MOFs-based nanoplatforms for self-enhanced imaging and treatment at tumor sites. Furthermore, the clinical research development of Fe-MOFs-based nanoplatforms is discussed, addressing key challenges and innovations for the future. Our review aims to provide novice researchers with a foundational understanding of advanced cancer theranostic modes and promote their clinical applications through the modification of Fe-MOFs.

1. Introduction

Cancer, a kind of high fatality rate disease, has been rapidly becoming the main cause of human death worldwide. Therefore, the development of effective cancer theranostic methods is a very urgent task at present. To date, novel therapeutic methods including chemodynamic therapy (CDT), photothermal therapy (PTT), photodynamic therapy (PDT), sonodynamic therapy (SDT) and immunotherapy with advantages of noninvasive and safe, have been broadly innovated to meet the increasing demands of clinical treatment [1–6]. However, these therapeutic approaches still encounter substantial challenges in cancer treatment. For instance, PDT faces challenges such as poor stability of photosensitizers and a high dependency on oxygen consumption within the tumor microenvironment (TME). In addition, CDT is limited by low concentration of tumor H_2O_2 and reduced glutathione (GSH). Hence, researchers devote themselves to explore suitable methods for improving cancer therapeutic outcomes. In recent decades, various advanced functional materials exhibiting multiple enzyme-like activities and other beneficial properties have been employed for cancer theranostics, aiming to achieve negligible side effects and high biosafety [7,8].

In the field of nanomedicine, metal-organic frameworks (MOFs) are extensively investigated for applications in drug delivery, detection of hazardous substances, bioimaging, biosensing, and cancer therapy [9–15]. The interests stem from their customizable morphology, adjustable specific surface areas, and advantageous physicochemical properties [16–19]. Due to inherent characteristics, including adjustable structure, biocompatibility, and electrochemical features suitable for cancer detection, MOFs have become a highly promising candidate for cancer therapy [20–22]. Diverse

* Corresponding author.
E-mail address: xujiating66@163.com (J. Xu).

https://doi.org/10.1016/j.cclet.2024.110501
1001-8417/

MOF-based nanoplatforms have been developed and built to satisfy the various needs of cancer therapy. For example, porphyrin-based MOF, a type of photosensitizers, possess intrinsic capacity for generating singlet oxygen ($^1O_2$) for PDT. In view of the diversity of inorganic metal ions and organic ligands, great opportunities are provided for the further functionalization of MOFs. By means of pre-functionalizing and post-synthetically altering the linkers and metal nodes of MOFs using organic molecule [23], inorganic nanoparticles (NPs) [24] and other active substances [25], it becomes possible to significantly enhance their anticancer efficiency. Moreover, tumor site can be targeted by MOFs because the size-related enhanced permeability and retention (EPR) effect. To enhance targeting efficiency and responsiveness in cancer therapy, MOFs are functionalized with specialized entities such as active targeting molecules, supramolecular nanovalves, biomacromolecules, and cell membranes. The achievement stems from the coordinated effect of metal nodes and the covalent coupling of organic ligands carrying functional groups (such as -NH_2 and -COOH) on the surface of MOFs [26–28]. Further, MOFs possess the ability to degrade in acidic TME, and ultimately be eliminated from the body, indicating their enormous promise in the field of biomedicine [29].

Among numerous MOFs, iron-based MOFs (Fe-MOFs) have received extensive attention from researchers due to their photosensitizer properties, peroxidase (POD)-like capability, imaging performance and good degradability [30,31]. Moreover, the low toxicity has further broadened the biological applications of Fe-MOFs. Fe-MOFs have Fe unsaturated metal centers with dense energy, which encouraged the oxygen atoms to establish coordination bonds with Fe^{III}. The stability and biocompatibility of Fe-MOFs attribute to the Fe^{III} acting as Lewis acid and the organic ligands acting as Lewis base [32,33]. However, they also possess inherent defects, such as the single treatment mode, limited electron transfer rate, insufficient cycle of Fe^{II}/Fe^{III}. To our knowledge, new chemical and physical properties of Fe-MOFs can be induced by the synergistic effect of integrating various materials, which provide additional active sites to significantly surpass the performance of pristine Fe-MOFs [34]. Recently, Fe-MOFs have been investigated as host matrices for integrating other nanohybrids, including various nanoparticles, organic compounds, metallic oxides, and polymers, thereby endowing Fe-MOFs with new properties [35–38]. These derived materials from Fe-MOFs significantly enhance capability of cancer theranostics and improve the biocompatibility of pristine Fe-MOFs [39].

So far, the use of nanohybrids combining with MOFs for anticancer catalytic applications has been widely researched and documented [7,40–42]. Numerous reviews on MOFs composites for bio-applications have also been published, such as drug delivery [43,44], biomimetic catalysis [45] and imaging *in vivo* [46]. Different from earlier works, the review focuses on the recent progress of engineered Fe-MOFs derived nanoplatforms for cancer theranostics (Table 1) [47–101]. The decorated organic molecules or inorganic NPs could not only enhance the therapy efficiency by synergistic effect with Fe-MOFs, but also endow the derived materials with imaging guidance and physical response ability. In detail, we summarized, categorized, exemplified and discussed about how they could be utilized in self-enhanced bioimaging and cancer catalytic therapy (Fig. 1). Finally, the challenges and prospects of Fe-MOFs-based nanoplatforms are comprehensively discussed to provide insights into their potential applications in cancer theranostics.

2. Organic molecule modified Fe-MOFs

The Fe-MOFs (Fig. S1 in Supporting information), which have got abundant attention due to their low toxicity, good biocompatibility, biodegradability and pH responsiveness, are novel nanomaterials for cancer catalytic theranostics [20,102–106]. Fe-MOFs have the ability to respond to endogenous GSH, releasing Fe^{II} and inducing Fenton/Fenton-like reactions to produce toxic hydroxyl radicals (•OH) in TME, thereby efficiently killing tumors. More significantly, Fe-MOFs can suppress the expression of glutathione peroxidase 4 (GPX4) and accelerate the accumulation of lipid peroxides (LPO), thereby triggering LPO-mediated ferroptosis [107,108]. The integration of organic molecules into Fe-MOFs results in multiple modes of tumor inhibition [16]. Therefore, Fe-MOFs may serve as robust platforms for constructing all-in-one theranostics systems in future.

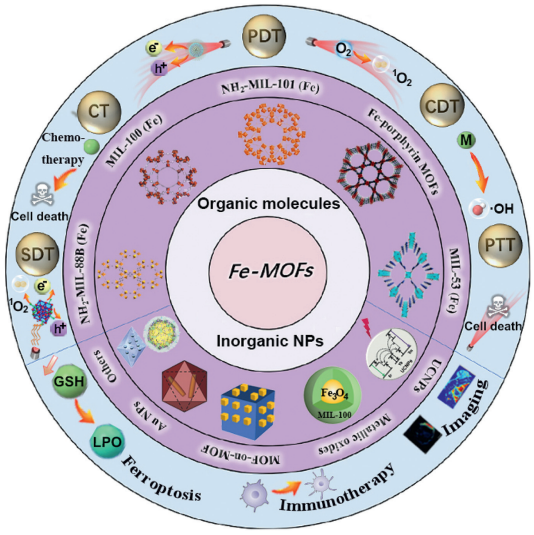

Fig. 1. Schematic diagram of engineered Fe-MOFs-based nanoplatforms for efficient cancer theranostics.

2.1. NH_2-MIL-88B(Fe)

NH_2-MIL-88B(Fe) is a widely studied isoreticular MOF in biomedicine, composed of topological trimeric secondary building units [109,110]. The trimers of μ_3O-bridged Fe^{III} octahedra [$Fe_3O(COO)_6$] that are used to build the structure of NH_2-MIL-88B(Fe) [$Fe_3O(solvent)_3Cl[NH_2C_6H_3(COO)_2]_3$·msolvent]. These trimers are further coupled by 2-aminoterephtalic acid (NH_2-BDC) ligands [111,112]. NH_2-MIL-88B(Fe), with intrinsic POD-like performance and well-known flexibility, has been chosen as a fundamental nano-catalytic therapeutic agent to initiate the entire therapeutic procedure [113,114].

In 2023, Qin and colleagues synthesized NH_2-MIL-88B(Fe), which was etched using thiamine pyrophosphate (TPP) and modified by autophagy agonist-chitosan oligosaccharides (COS) for creating COS@MOF [2]. Initially, the therapeutic technique was shown in Fig. 2a that employed disrupting intracellular iron homeostasis for tumor catalytic treatment in conjunction with ferroptosis. In the synthetic process, TPP, as an organic weak acid, slowly released abundant protons to etch the unprotected surface of MOF *via* destroying coordination bonds. The unique hollow structure exposes more active sites, facilitating the adsorption of overexpressed H_2O_2 in the TME and enhancing POD-like activity for reactive oxygen species (ROS) generation. Fig. 2b illustrates the octahedral shape and uniform size of the MOF, as observed by transmission electron microscopy (TEM). When the molar mass ratio of MOF to TPP was 1:2.5 (designated as COS@MOF (1:2.5)), the most pronounced cavity structure was revealed, prompting its use in a series of studies (Fig. 2c).

Autophagy and ferroptosis-related proteins were further identified by western blotting (Fig. 2d). The COS@MOF (1:2.5) group

Table 1
Examples of Fe-MOF-based nanoplatforms for combination cancer therapy, including bimodal and multimodal therapy.

Pristine Fe-MOF	Name of nanoplatform	Application[s]	*In vivo* model	Refs.
NH_2-MIL-88B(Fe)	COS@MOF	CDT/ferroptosis	CT26 tumor-bearing mice	[2]
NH_2-MIL-88B(Fe)	CGMOF@CA@HA	CDT/PDT, MRI	U14 tumor-bearing mice	[47]
NH_2-MIL-88B(Fe)	MPG	CDT/SDT/starvation therapy	4T1 tumor-bearing mice	[48]
NH_2-MIL-88B(Fe)	D-/L-Cu_xOS@Fe-MOFs	CDT/ferroptosis/cuproptosis	4T1 tumor-bearing mice	[49]
NH_2-MIL-88B(Fe)	MOF(Fe)+CQ	CDT/autophagy inhibition	HeLa tumor-bearing mice	[50]
NH_2-MIL-88B(Fe)	DOX@MOF-COD@CS	CDT/chemotherapy	MCF-7 tumor-bearing mice	[51]
NH_2-MIL-88B(Fe)	^{125}I-MIL-88B(Fe)	CDT	Panc-1 tumor-bearing mice	[52]
MIL-88B(Fe)	MIL-88-ICG@ZIF-8DOX	Chemotherapy/PDT/PTT; FLI	4T1 tumor-bearing mice	[53]
MIL-88B(Fe)	UMP	CDT/PDT	U87MG tumor-bearing mice	[54]
MIL-88A(Fe)	Au@MIL-88A(Fe)	CTI/MRI/PAI	U87 MG-subcutaneous tumor-bearing mice	[55]
MIL-100(Fe)	AMP NRs	CDT/PTT; PAI	4T1 tumor-bearing mice	[35]
MIL-100(Fe)	IMF	CDT/PDT/ferroptosis, PAI and FLI	4T1 tumor-bearing mice	[38]
MIL-100(Fe)	NMIL-100@GOx@C	CDT/chemo-/starvation therapy/ferroptosis; FLI	4T1 tumor-bearing mice	[56]
MIL-100(Fe)	MOF@HA@ICG	CDT/PTT, PAI/MRI/FLI	MCF7 tumor-bearing mice	[57]
MIL-100(Fe)	Oxa@MIL-PDA-PEGTK	Chemotherapy/CDT/PTT, PTI	PRF/5 tumor-bearing mice	[58]
MIL-100(Fe)	PPy@MIL-100-DOX	Chemotherapy/PTT	—	[59]
MIL-100(Fe)	OIMH	Chemo-/immuno-therapy/PTT, PAI	CT26 tumor-bearing mice	[60]
MIL-100(Fe)	DMH	Chemotherapy/CDT	MCF7 tumor-bearing mice	[61]
MIL-100(Fe)	MCM@PEG-CO-DOX	Chemo-/immuno-therapy/PTT, PAI, MRI	HCT116 tumor bearing mice	[62]
MIL-100(Fe)	PCMGH	CDT/PTT/starvation therapy	U87 tumor-bearing mice	[63]
MIL-100(Fe)	MGH	CDT/PTT/starvation therapy, PAI	4T1 tumor-bearing mice	[64]
MIL-100(Fe)	MMC	Chemotherapy/CDT, FLI	JEG-3 tumor-bearing mice	[65]
MIL-100(Fe)	CMH	CDT/PDT, FLI	4T1 tumor-bearing mice	[66]
MIL-100(Fe)	FMG	CDT/starvation therapy	4T1 tumor-bearing mice	[67]
MIL-100(Fe)	Z/D@MOF@MN	Chemotherapy/PDT, PTI	4T1 tumor-bearing mice	[68]
MIL-100(Fe)	FMUP	CDT/PDT, CTI/UCLI	U14 tumor-bearing mice	[69]
MIL-100(Fe)	UCNPs@MIL-100(Fe)@DOX	CDT/PTT/chemotherapy, UCLI/CTI/MRI	U14 tumor-bearing mice	[70]
MIL-100(Fe)	FMUP	CDT, MRI/UCLI	HeLa tumor-bearing mice	[71]
NH_2-MIL-101(Fe)	GDMCN2	SDT/ferroptosis/chemo, FLI	PANC-1 tumor-bearing mice	[37]
NH_2-MIL-101(Fe)	ICG-CpG@MOF	CDT/PDT/PTT/immunotherapy, FLI/PAI/PTI/MRI	4T1 tumor-bearing mice	[72]
NH_2-MIL-101(Fe)	FeOA	CDT/immunotherapy	B16 tumor-bearing mice	[73]
NH_2-MIL-101(Fe)	NH_2-MIL-101(Fe)/CPT-11	Chemotherapy/CDT	MCF7 tumor-bearing mice	[74]
NH_2-MIL-101(Fe)	HG-MIL@PDANPs	CDT/PTT, FLI, PTI	MDA-231 tumor-bearing mice	[75]
NH_2-MIL-101(Fe)	MOF-Pt(IV)@GOx	Chemo-/starvation therapy/ferroptosis/CDT	4T1 tumor-bearing mice	[76]
NH_2-MIL-101(Fe)	DOX@MIL-LOX@AL	CDT/chemo-/immunotherapy, FLI	4T1 tumor-bearing mice	[77]
NH_2-MIL-101(Fe)	P@M	CDT/PTT	HepG2 tumor-bearing mice	[78]
NH_2-MIL-101(Fe)	MNMCF	CDT/PDT	4T1 tumor-bearing mice	[79]
NH_2-MIL-101(Fe)	CPMP	CDT/SDT/ferroptosis	4T1 tumor-bearing mice	[80]
NH_2-MIL-101(Fe)	UMP-FA	UCLI/MRI	KB tumor-bearing mice	[81]
NH_2-MIL-101(Fe)	BQ-MIL@cat-MIL	PTT/PDT	HeLa tumor-bearing mice	[82]
MIL-101(Fe)	MIL-101(Fe)@BSA-AuNCs	MTT/MEDT, MRI, FLI	H22 tumor-bearing mice	[83]
MIL-101(Fe)	MCDP@Bif	Chemotherapy/CDT	4T1 tumor-bearing mice	[84]
MIL-101(Fe)	Se/Ru@MIL-101	Chemotherapy	MCF7 tumor-bearing mice	[85]
MIL-53(Fe)	MIL-53@CM-272	CDT/SDT/ferroptosis/immunotherapy	MB49 tumor-bearing mice	[36]
MIL-53(Fe)	MIL-53@F^-@M	CDT/chemotherapy	H22 tumor-bearing mice	[86]
MIL-53(Fe)	FCSDG	CDT/chemo-/starvation therapy	4T1 tumor-bearing mice	[87]
MIL-53(Fe)	Tb-MOF-on-Fe-MOF	Biosensor	—	[88]
PCN-600(Fe)	CaP@Fe-MOFs	CDT/immunotherapy	4T1 tumor-bearing mice	[89]
PCN-600(Fe)	PCN-DOX@PDA	PDT/PTT/chemotherapy, MRI	4T1 tumor-bearing mice	[90]
PCN-222(Fe)	UPFB	CDT/PDT/SDT, MRI	U14 tumor-bearing mice	[91]
PCN-222(Fe)	UMOFs@Au	CDT/PDT/starvation therapy	U87MG tumor-bearing mice	[92]
PCN-224(Fe)	DFMSL	CDT/SDT/ferroptosis, UCLI/MRI	C6 tumor-bearing mice	[93]
Fe-GA	UCNP@GA-Fe^{III}	PTT/ferroptosis, MRI/UCLI	Colorecta tumor-bearing mice	[94]
Fe-tannic acid	SFT-MB	PDT/CDT/ferroptosis	4T1 tumor-bearing mice	[95]
Fe-epigallocatechin-3 gallate	PTCG	CDT/chemotherapy	HepG2 tumor-bearing mice	[96]
Fe-artemisinin	Fe(III)-ART	CDT, MRI	A549 tumor-bearing mice	[97]
Fe-gossypol	PFGs	PDT/immunotherapy, FLI	4T1 tumor-bearing mice	[98]
Fe-anthocyanins	FeAP-NPs	PTT, MRI/PAI	MCF7 tumor-bearing mice	[99]
Fe-ellagic acid	Fe-EA NPs	PTT, MRI	4T1 tumor-bearing mice	[100]
Fe-dopamine	PtH@FeP	CDT/ferroptosis, MRI/FLI	4T1 tumor-bearing mice	[101]

showed the lowest GPX4 expression among all groups, attributing to overexpressed the autophagy of ferritin and inducing ferroptosis [115]. CT26 tumor-bearing mice were used to assess the therapeutic capacity of COS@MOF (1:2.5) *in vivo*. Among the four experimental groups, tumor growth was significantly inhibited in the COS@MOF-treated group. In contrast to the control group, mice injected with COS and MOF showed only slight decrease in tumor growth (Fig. 2e). Overall, COS@MOF holds great promise for engineering Fe-MOFs in the treatment of colorectal cancers, leveraging highly effective synergistic nanocatalytic/ferroptosis therapy.

In our recent report [47], a nano-photosensitizer was fabricated by incorporating Cu^{2+} and gallic acid (GA) into the biodegradable NH_2-MIL-88B(Fe) (CGMOF) to create Fe-O(GA)-Cu ligand-to-metal charge transfer (LMCT) bridge bond, which effectively inhibited the recombination of electron/hole (e^-/h^+) pairs during PDT under 650 nm laser irradiation and accelerated the Fe^{II}/Fe^{III} redox cycles for CDT. Cinnamaldehyde (CA) was grafted onto CGMOF for tumor-responsive hydrogen peroxide self-supply (CGMOF@CA). Subsequently, hyaluronic acid (HA) was surface-modified (CGMOF@CA@HA) to achieve the targeted delivery (Fig. 3a). The TEM images displayed in Fig. 3b indicated that the size of CGMOF was

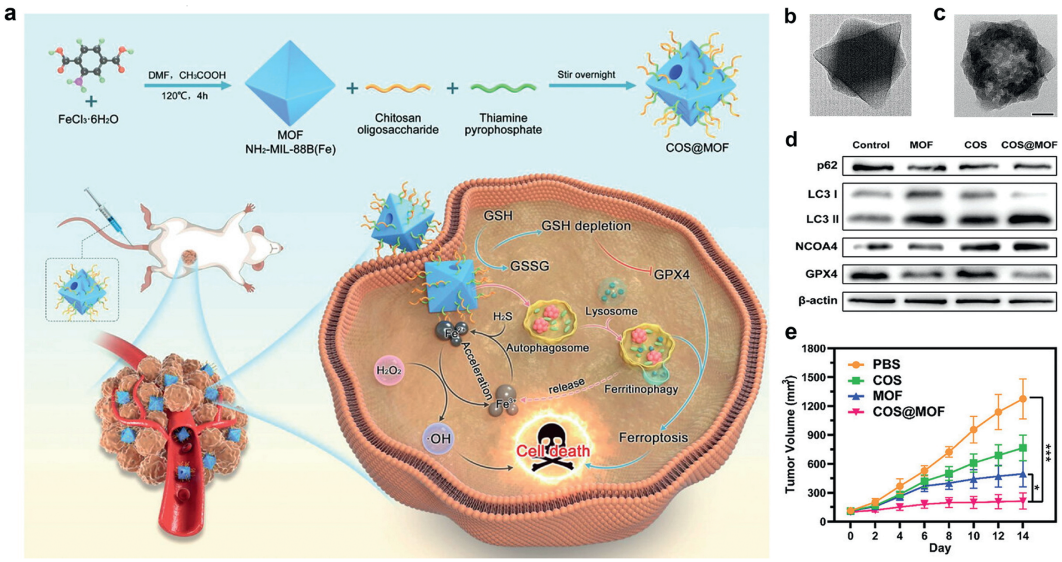

Fig. 2. (a) Schematic diagram of an engineered MOF with amplifying autophagy to enhance ferroptosis for nanocatalytic tumor therapy. (b, c) TEM images of MOF [NH_2-MIL-88B(Fe)] and COS@MOF with different proportions of TPP (1:2.5) (Scale bar: 50 nm). (d) Western blot of autophagy and ferroptosis-related proteins in CT26 cells. (e) Tumor volume of dissected tumors of CT26-bearing nude mice after different treatments, including PBS, COS, MOF, and COS@MOF. Reproduced with permission [2]. Copyright 2023, Wiley-VCH GmbH.

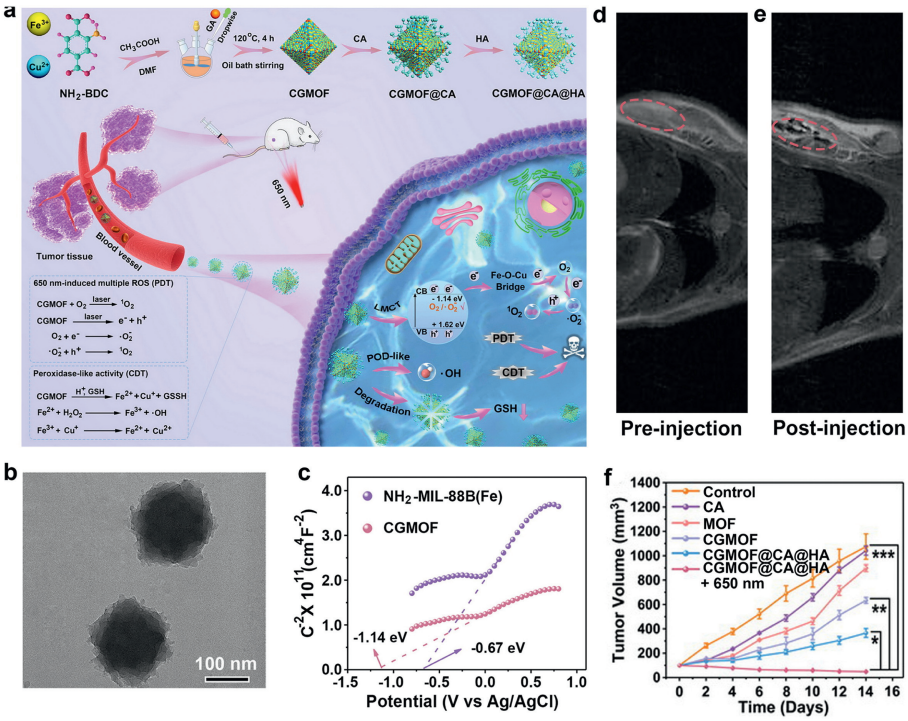

Fig. 3. (a) Schematic illustration of the synthetic procedures and the therapy mechanism of the CGMOF@CA@HA. (b) TEM image of CGMOF. (c) Mott-Schottky plots of NH_2-MIL-88B(Fe) and CGMOF. *In vivo* T_2-weighted MRI of tumor-bearing mice before (d) and after (e) injection of CGMOF@CA@HA. (f) Relative tumor volume changes of U14 tumor-bearing mice with different treatments. Reproduced with permission [47]. Copyright 2024, Elsevier Inc.

approximately 225 nm. To demonstrate the role of the Fe-O(GA)-Cu LMCT bridge bond, electrochemical tests were performed to assess the carrier density of CGMOF. Importantly, Mott-Schottky curves obtained at 1000 Hz revealed that the carrier density of CGMOF was 2.74 times higher than that of MOF, confirming that CGMOF exhibited enhanced efficiency in the separation of e^-/h^+ pairs (Fig. 3c). *In vivo* experiments using U14 tumor-bearing mice were conducted to investigate the distribution of CGMOF@CA@HA within a living organism. The T_2-weighted magnetic resonance imaging (MRI) signal was noticeably increased at the tumor site following the injection of CGMOF@CA@HA into U14 tumor bearing mice, providing realtime information for cancer theranostics (Figs. 3d and e). Furthermore, both PDT and CDT performance of the CGMOF@CA@HA were evaluated (Fig. 3f). In the six groups, the tumors were successfully suppressed in mice treated with CGMOF@CA@HA plus 650 nm laser irradiation, whereas tumor growth in mice injected with CGMOF@CA@HA without laser irradiation was only minimally suppressed compared to the control group.

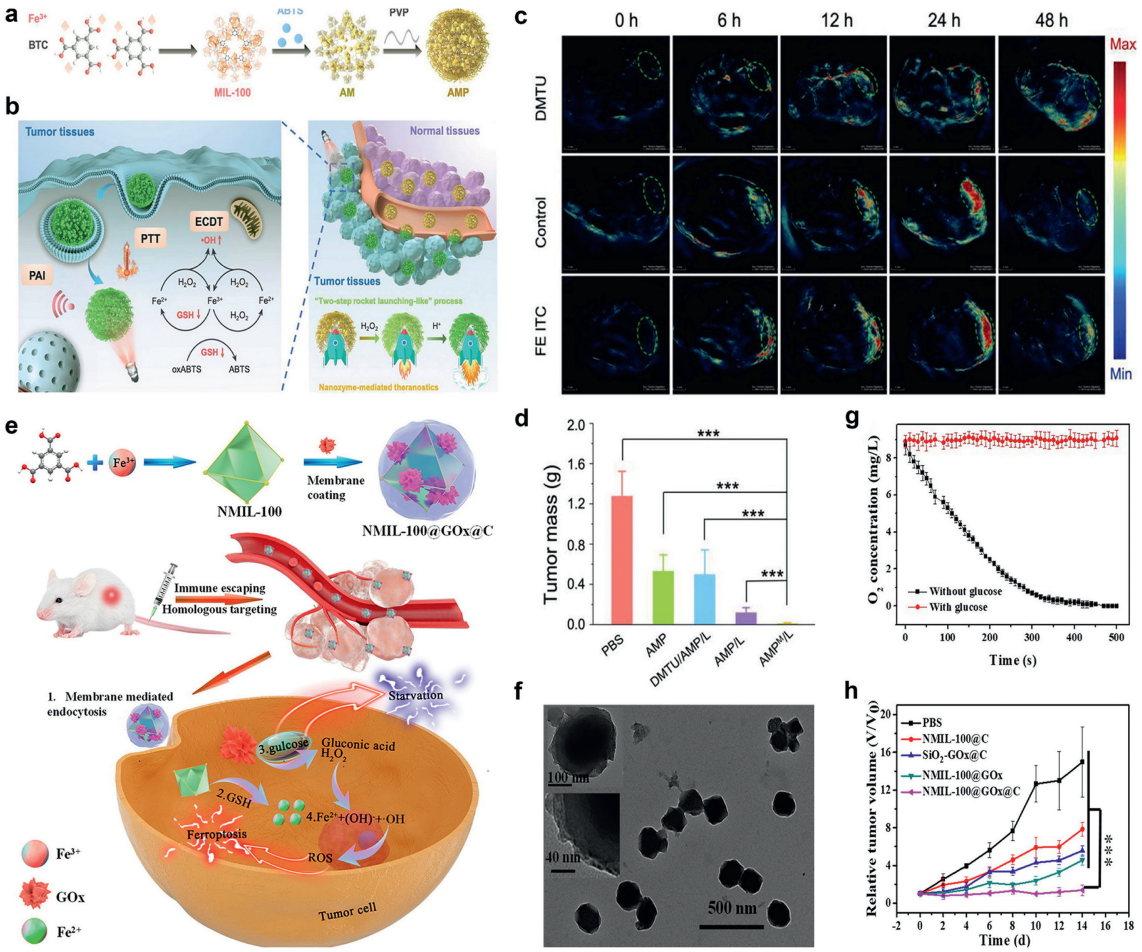

Fig. 4. (a) Preparation procedure of AMP NRs. (b) Schematic illustration of AMP NRs for tumor-microenvironment-activated nanozyme-mediated theranostics. (c) Representative PAI images of tumor with different treatments as a function of postinjection time of AMP NRs. (d) The average tumor mass of excised tumors of different groups on the 14th day. Reproduced with permission [35]. Copyright 2019, Wiley-VCH Verlag GmbH & Co. KGaA, Weinheim. (e) Schematic illustration of the preparation of NMIL-100@GOx@C and the cascade processes for cancer therapy. (f) TEM images of NMIL-100@GOx@C. (g) O_2 concentration variations of NMIL-100@GOx@C solution with or without glucose. (h) Tumor growth curve after the mice receiving different treatments. Reproduced with permission [56]. Copyright 2020, American Chemical Society.

In addition to the works mentioned above, there are other research studies on modifying NH_2-MIL-88B(Fe) or MIL-88B(Fe) for enhancing cancer theranostics [48–54]. NH_2-MIL-88B(Fe) and MIL-88B(Fe) possess inherent POD-like performance and visible light responsiveness, making it a compelling candidate for the development of novel cancer theranostics agents in the foreseeable future.

2.2. MIL-100(Fe)

MIL-100(Fe) ($[Fe_3O(H_2O)_2(OH)(BTC)_2]$), another type of Fe-MOFs, was widely studied in field of antitumor [116]. MIL-100(Fe) consists with oxo-centered trimer unit that coordinates with two unsaturated metal sites, which could be applied for CDT owing to its intrinsic POD-like performance [117–119]. In 2019, Chen *et al.* designed a nanoplatform by loading 2,2′-azino-bis(3-ethylbenzothiazoline-6-sulfonic acid) (ABTS) into MIL-100(Fe) [35]. Subsequently, poly(vinylpyrrolidone) (PVP) and cancer cell membranes were coated onto ABTS@MIL-100 to fabricate activatable ABTS@MIL-100/PVP nanoreactors (AMP NRs), enabling integration of photoacoustic imaging (PAI) combined CDT with PTT (Figs. 4a and b). 4T1 tumor-bearing mice were intravenously injected with AMP NRs to confirm that PA signal of in tumor sites existed H_2O_2 concentration dependent behavior (Fig. 4c). Furthermore, as shown in Fig. 4d, the tumor mass graphs demonstrated the good antitumor performance of AMP NRs *in vivo*.

In addition, Tang *et al.* constructed MIL-100(Fe) that loaded with glucose oxidase (GOx), which was further coated with cancer cell membrane to form a cascade catalysis nanoreactor (NMIL-100@GOx@C), which integrated the function of CDT, ferroptosis and starvation therapy [56]. Such nanoreactor degrade in response to overexpressed GSH at tumor region, thus the released GOx to catalyze the oxidation of glucose for H_2O_2 generation *in situ*, making up for the lack of H_2O_2 to accelerate Fe cycle and facilitate $^{\bullet}OH$ production (Fig. 4e). The TEM images of corresponding samples were displayed in Fig. 4f, exhibiting that the outer surface of NMIL-100@GOx was coated cancer cell membranes. To assess the glucose decomposition capability, changes in O_2 content were measured during the catalytic reaction of GOx using a portable dissolved oxygen meter *in vitro*. As shown in Fig. 4g, when NMIL-100@GOx@C and glucose existed in the system, the concentration of O_2 reduced rapidly. These results not only validated that GOx was indeed a potent glucose disintegrant in NMIL-100@GOx@C, but they also showed that NMIL-100@GOx@C could be used to starve cancer cells for starvation therapy. Moreover, *in vivo* antitumor studies demonstrated that the NMIL-100@GOx@C group exhibited great antitumor performance, markedly inhibiting tumor growth (Fig. 4h). Other good works using MIL-100(Fe) to construct theranostics nanoarchitectures have also been reported [38,57–68].

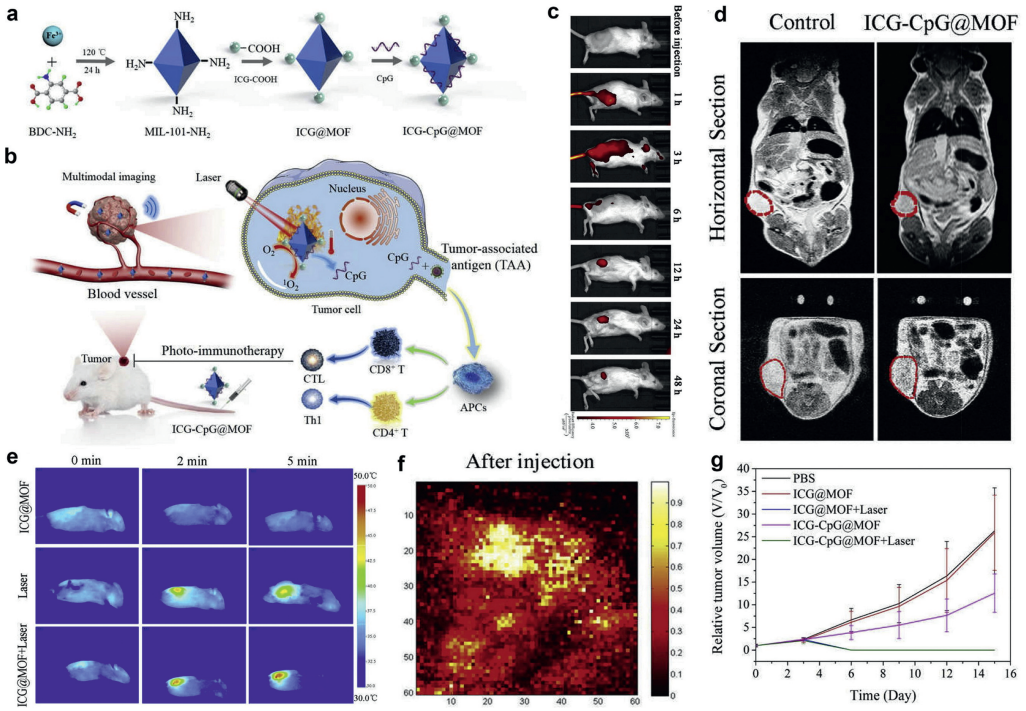

Fig. 5. Schematic illustration for (a) synthesis of ICG-CpG@MOF and (b) mechanism of multimodality imaging (PAI, MRI, FLI) guided synergistic cancer photo-immunotherapy. (c) Time series of the tumor near-infrared FLI *in situ* after tail vein injection for 0–48 h. (d) Horizontal section and coronal section MRI in tumor-bearing mice 2 h after *in situ* injection. (e) *In situ* PTI. (f) PAI of tumor after *in situ* injection. (g) Statistical analysis of tumor volume. Reproduced with permission [72]. Copyright 2020, The Authors.

2.3. NH_2-MIL-101(Fe)

MIL-101 [$Fe_3(\mu_3\text{–}O)Cl(H_2O)_2(BDC)_3$], with the three-dimensional structure of two holes cage, have been first synthesized by Ferey team in 2005 using terephthalic acid (H_2BDC) ligand [120]. Other researchers have successfully prepared abundant MOF materials, such as MIL-101(Fe), MIL-101(Al), MIL-101(Ti) and MIL-101(V) through replacement of metal elements in subsequent research work [121]. Notably, MIL-101(Fe) has active valence conversion of Fe^{II}/Fe^{III} and the excellent ligand-metal charge transfer capability, thus it has well application prospect in CDT and PDT [122–125].

Beginning with iron, Bauer *et al.* pioneered research that effectively synthesized amino-functionalized MIL-101(Fe) (NH_2-MIL-101(Fe)) [110]. Afterwards, Liao *et al.* employed NH_2-MIL-101(Fe) as a key carrier to construct cancer photoimmunotherapy nanoplatform with multimodal imaging function [72]. The donors of fluorescent signal (indocyanine green, ICG) and immune adjuvants (cytosine-phosphate-guanine sequence, CpG) were co-loaded into the framework of NH_2-MIL-101(Fe) (named as ICG-CpG@MOF). Such nanocarriers could passively accumulate at the lesion sites *via* the EPR effect, enabling multimodal tumor imaging. Under 808 nm laser irradiation, cancer immunotherapy combining PDT and PTT were achieved (Figs. 5a and b).

A clear fluorescence imaging (FLI) signal was observed at the tumor site, reaching its peak intensity 3 h after intravenous injection and showing a significant decrease after 24 h (Fig. 5c). Moreover, MRI (Fig. 5d), photothermal imaging (PTI) (Fig. 5e), and PAI (Fig. 5f) were notably enhanced in the tumor region upon injection of ICG-CpG@MOF. Benefiting from its outstanding multimodal imaging capabilities, *in vivo* antitumor assays were conducted to evaluate the PTT, PDT and photoimmunotherapy performance of ICG-CpG@MOF. After 21 days treatment, the tumor volume in the group of ICG-CpG@MOF was obviously inhibited compared to other groups (Fig. 5g). In conclusion, the combination of CpG, ICG, and Fe-MOFs not only released tumor-related antigens to stimulate the immune system, enhancing tumor cytotoxicity, but also enabled multimodal imaging, thereby achieving high cure rates. Numerous other nanostructures based on NH_2-MIL-101(Fe) have been fabricated and extensively investigated for applications in cancer theranostics [73–80,83]. For future anticancer research work, a possible avenue to design novel nanoplatforms might modify NH_2-MIL-101(Fe) using organic molecules.

2.4. MIL-53(Fe)

MIL-53(Fe), a kind of three-dimensional porous Fe-MOFs, is construct by infinite one-dimensional linkage of -Fe-O-O-Fe-O-Fe- from H_2BDC ligands and Fe^{III} [126]. MIL-53(Fe), which exhibits intrinsic catalase (CAT)-like and sonosensitizer properties, enhances the efficiency of SDT by catalyzing the generation of oxygen. Additionally, the Fe-MOF boasts a remarkably large surface area and biodegradable in response to TME, making it ideal for loading chemotherapy drugs. In 2023, Yang and colleagues designed a nanoplatform (MIL-53@CM-272) with triple antitumor functions-ferroptosis, apoptosis, and immunogenic cell death (ICD) for bladder cancer therapy. The nanoplatform was constructed by loading the chemotherapy drug (CM-272) into MIL-53(Fe) (Figs. 6a and b) [36].

TEM image demonstrated the fusiform morphology of MIL-53 with a consistent size of ~100 nm (Fig. 6c). Further, the energy band structure of MIL-53@CM-272 was analyzed to elucidate the mechanism for serving as a sonosensitizer to generate ROS. Initially, the bandgap (E_g) was calculated to be 2.72 eV by Tauc plot (Fig. 6d), and the valence band potential (E_{VB}) of MIL-53@CM-272 was measured to be 2.25 eV *via* XPS valence band spectrum (Fig. 6e). Therefore, conduction band potential (E_{CB}) was confirmed as −0.47 eV according to the formula $E_{CB} = E_{VB} - E_g$. The E_{VB} of MIL-53@CM-272 was more positive than E^{θ} ($H_2O/^{\bullet}OH$, +2.01 eV), indicating that hole have ability to convert H_2O into $^{\bullet}OH$ under ultrasound (US) irradiation (Fig. 6f). In addition, E_{CB} of MIL-53@CM-

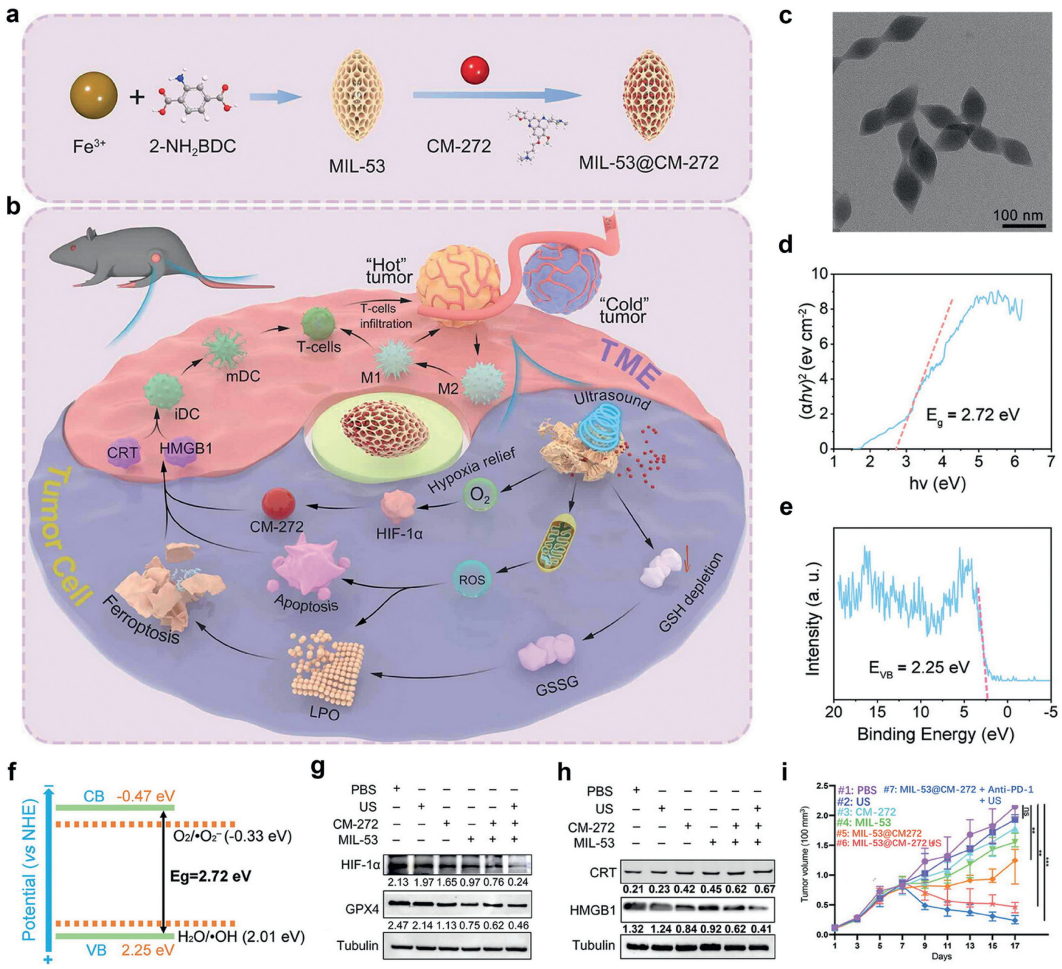

Fig. 6. (a) Schematic representation of the synthesis of MIL-53@CM-272. (b) Multiple functions of MIL-53@CM-272 in the TME and under US stimulation. MIL-53@CM-272 + US induces tumor cell apoptosis and ferroptosis, facilitating the provision of O_2 to enhance ICD in an immune microenvironment. (c) TEM images of MIL-53. (d) Plot of $(ahv)^2$ against photon energy (hv) to obtain the band gap. (e) Measured valance band of MIL-53@CM-272 obtained using XPS analysis. (f) Schematic of the energy band structure of MIL-53@CM-272 *versus* $H_2O/^{\bullet}OH$, and $O_2/^{\bullet}O_2^-$ redox potentials. (g) Western blot results of HIF-1α, GPX4, expression levels in MB49 cells after different treatments. (h) HMGB1 and CRT protein levels after different treatments. Quantitative of Western blot results were labeled under the line. (i) Primary tumor growth curve after the mice receiving different treatments after 17 days. Reproduced with permission [36]. Copyright 2023, Wiley-VCH GmbH.

272 was less than E^{θ} ($O_2/^{\bullet}O_2^-$, −0.33 eV), revealing that superoxide radicals ($^{\bullet}O_2^-$) can be produced by this path. Therefore, the apoptosis can be occurred owing to the generation of ROS.

According to previous study, the accumulation of LPO and the expression reduction of GPX4 can induce ferroptosis [127]. Western blot analysis was used to evaluate expression of GPX4 in MB49 cells (Fig. 6g). In the MIL-53@CM-272 + US group, the lowest GPX4 expression among all groups was clearly exhibited, indicating that MIL-53@CM-272 was a good agent for ferroptosis. Furthermore, compared to the other groups, the MIL-53@CM-272 + US group also demonstrated the greatest ability to reduce the expression of hypoxia-inducible factor-1α (HIF-1α), confirming that MIL-53@CM-272 + US can alleviate hypoxic conditions and enhance SDT in the TME.

ICD process was triggered by releasing danger signals including high-mobility group box 1 (HMGB1) and calreticulin (CRT), which can improve antitumor immune responses. As shown in Fig. 6h, the expression of HMGB1 and CRT after different treatments were confirmed using Western blot. When MB49 cells were treated with MIL-53@CM-272 + US, the level of HMGB1 significantly decreased compared to the CM-272 or MIL-53 alone groups. Conversely, the level of CRT was increased, suggesting that MIL-53@CM-272 + US enhanced ICD by synergistically inducing ferroptosis in an oxygen-sufficient environment. Excitingly, MB49 tumor-bearing mice treated with MIL-53@CM-272 + US exhibited significant tumor suppression, attributing to the combined therapeutic effects of apoptosis, ferroptosis, and ICD (Fig. 6i). Additionally, other materials derived from MIL-53(Fe) were successfully developed by enclosing the organic molecules for enhancing cancer theranostics [86–88].

2.5. Fe-porphyrin MOFs

Iron and tetrakis(4-carboxyphenyl)porphyrin (TCPP) act respectively as the active site and heme-like ligand in constructing Fe-porphyrin MOFs, thereby maximizing their catalytic potential [89,104,128]. PCN-600(Fe) (PCN stands for porous coordination network) is known for its large porosity, frequently utilized by researchers for loading chemotherapy drug [1,129,130]. Zhang *et al.* developed the nanoplatform (PCN-DOX@PDA), constructed using PCN-600(Fe) as a carrier for transporting polydopamine (PDA) and chemotherapy drugs. PDA was used as photothermal agent of PTT by near-infrared laser irradiation, and TCPP was employed as agent of generating $^1O_2$ under 633 nm laser irradiation. Additionally, since the central ion of PCN is Fe^{III} and ligand of TCPP, PCN-DOX@PDA realized MRI-mediated CDT, PDT and PTT at tumors region (Fig. 7a) [90]. To assess the degradability under TME, the TEM images of PCN-DOX@PDA at pH 7.4 and 5.4 were displayed in

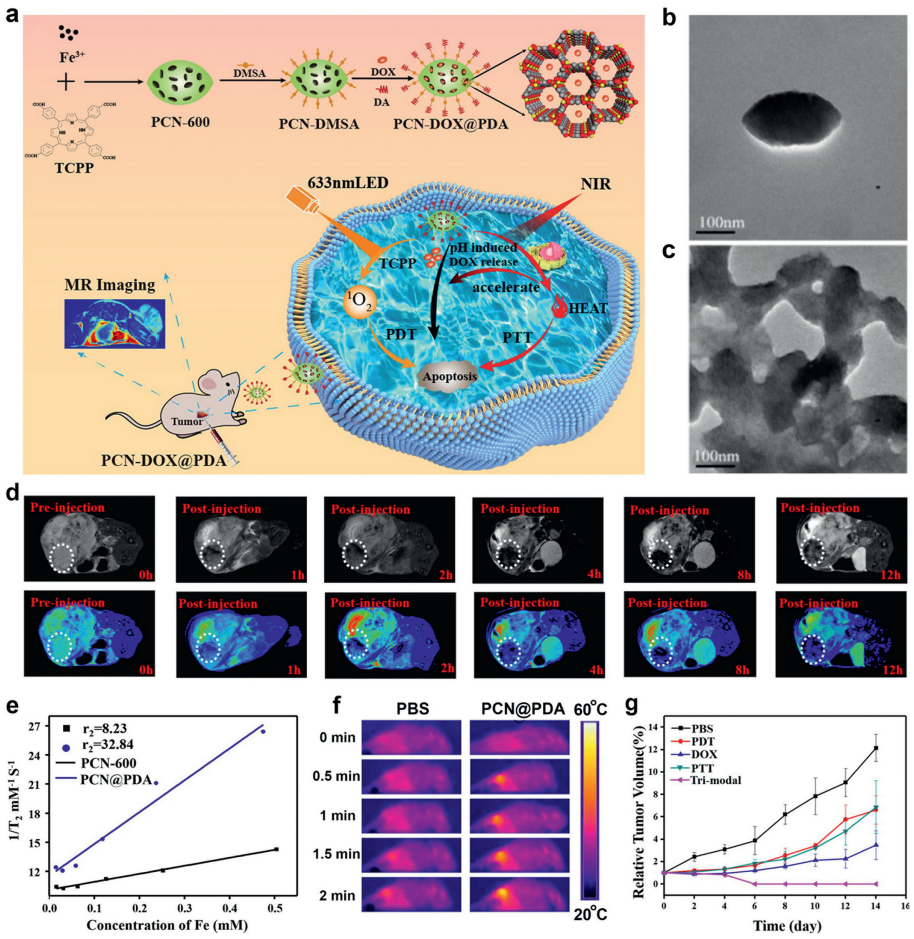

Fig. 7. (a) Illustration of the design of PCN-DOX@PDA and the lethal mechanism model of PCN-DOX@PDA against tumor cells. (b) TEM image of PCN-DOX@PDA NPs. (c) PCNDOX@PDA NPs under acidic condition (pH 5.4). (d) *In vivo* T_2-weighted MR imaging at different intervals after intratumoral injection of PCN-DOX@PDA NPs in 4T1-bearing mice; color images as shown below. White circles denote tumors. (e) T_2 relaxation rates (r_2) of PCN-600 and PCN-DOX@PDA NP solutions at various Fe concentrations. (f) Infrared thermography of PCN@PDA-injected tumor-bearing mice irradiated under an 808 nm laser (1.0 W/cm^2). (g) The relative tumor volume. Reproduced with permission [90]. Copyright 2023, American Chemical Society.

Figs. 7b and c, respectively. These results revealed that Fe^{III} can be released from PCN-DOX@PDA at pH 5.4, causing electron spin direction rearrangement of Fe^{III} and enhancing the T_2-weighted MRI performance.

The distribution of PCN-DOX@PDA in living organisms was investigated in 4T1 tumor-bearing mice. MRI revealed significant darkening at the tumor site (Fig. 7d). In Fig. 7e, the r_2 value increased approximately fourfold following the PDA coating, demonstrating the enhanced MR contrast capacity of PCN-DOX@PDA. Subsequently, the *in vivo* infrared thermography ability of PCN-DOX@PDA was investigated in living mice (Fig. 7f). Compared to PCN-DOX@PDA group, the temperature in the phosphate buffered saline (PBS) group increased negligibly at tumor region. Finally, *in vivo* antitumor assays were conducted on 4T1 tumor-bearing mice after intravenous injections of PCN-DOX@PDA. Following a 14-day treatment period, the tumor growth curves demonstrated a clear inhibition of tumor growth in mice treated by PCN-DOX@PDA (Fig. 7g).

3. Inorganic NPs modified Fe-MOFs

Fe-MOFs have been widely explored as basics to integrate various inorganic NPs for enhancing performance of catalytic therapy [131]. These emerging nanomaterials including upconversion nanoparticles (UCNPs) [94], metallic oxides [38,84,103], Au NPs [55], covalent organic framework (COF) [37], quantum dots (QDs) [132] and the structure of MOF-on-MOF [133–135] serve as guest NPs to incorporate additional functionalities into Fe-MOFs, which will be discussed in present section.

3.1. UCNPs

The most commonly researched ligands of Fe-MOFs are "bioinert", which poses challenges in creating highly biocompatible treatment systems [136]. Building completely functional bio-MOFs with active natural polyphenols ligands acting as anticancer nanomaterials have a lot of potential [137–139]. For instance, GA, a type of natural polyphenol, exhibits a strong coordination chelating effect with certain transition metal ions [140–143]. Additionally, the electronic d-d transition between GA and Fe^{III} causes GA-Fe^{III} complexes to exhibit broad absorption in the near-infrared region, resulting in clear photothermal effects [144–146]. In 2019, Gao *et al.* developed that the complex of GA-Fe^{III} coated UCNP (named as UCNP@GA-Fe^{III}) to integrate PTT, MRI and upconversion luminescence imaging (UCLI) [94]. Owing to the introduction of an unsaturated coordination structure, Fe^{III} in the nanoprobe can be selectively released only in the TME in response to the slightly acidic pH. UCLI was employed to quantitatively visualize the release of Fe^{III} *in vivo*, whilst the release resultant serves as a photothermal agent to integrate the diagnosis and treatment (Fig. 8a).

To validate the tumor accumulation ability, UCNP@GA-Fe^{III} NPs were intravenously injected into human colorectal cancer

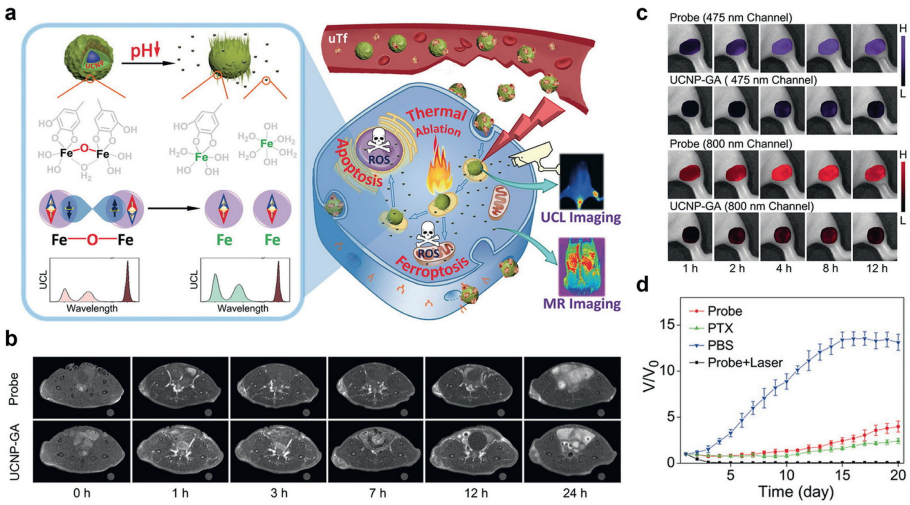

Fig. 8. (a) Illustration to demonstrate the activatable function of UCNP@GA-Fe^{III} probe for MRI and its therapeutic function involving multiple pathways. (b) T_1-weighted MRI of tumor-bearing mice acquired at different time points pre- and post-injection of the probe and UCNP-GA control, respectively. (c) UCLI of the tumor site acquired through different imaging channels (475 and 800 nm), overlaid with the bright field images. (d) Tumor growth curves of different treatments during a therapy course. Reproduced with permission [94]. Copyright 2019, Wiley-VCH Verlag GmbH &Co. KGaA, Weinheim.

xenografts to BALB/c nude-bearing mice. UCNP@GA-Fe^{III} probe exhibited stronger ability for targeting tumor sites compared to control group (Fig. 8b). As shown in Fig. 8c, the UCL through the 802 nm channel appeared at the tumor site 2 h post-injection of the UCNP@GA-Fe^{III} probes. The emission intensity steadily rose until it reached a plateau between 4 h and 8 h post-injection, followed by a slight decline upon extended observation. The UCL signal at 475 nm showed a similar trend, although the overall signal intensities of the UCNP@GA-Fe^{III} probes were significantly stronger than those recorded from the control (UCNP-GA). The results again demonstrated that apart from the EPR effect, the unsaturated transferrin-mediated recognition contributed to the UCNP@GA-Fe^{III} probe target tumor more effective *in vivo*. Importantly, after 20 days of treatment, the size of tumor was significantly reduced or eliminated with the use of the probes and laser (Fig. 8d). The delicate design of the probe offered a novel platform for monitoring the release of exogenous Fe^{III} ions for theranostics applications.

Lin *et al.* reported on the activation of UCNPs@PCN-224(Fe) (UPFB) heterodimer nanocomposites, which were responsive to both 808 nm laser and ultrasound. The dual activation mechanism facilitated the performance of both PDT and SDT [91]. Fe^{III} ions coordinated within TCPP can act as CAT-like nanozymes. The nanocomposites not only catalyzed the conversion of H_2O_2 to produce O_2, thereby alleviating hypoxia in the tumor microenvironment, but also effectively consumed intracellular GSH to mitigate the impact of ROS generation for CDT. Biotin was utilized to functionalize the surface of the nanocomposites, enabling their rapid accumulation in tumor regions to augment theranostics effectiveness. After 14 days of synergetic treatment, U14 tumor-bearing mice exhibited nearly no tumor growth, indicating the substantial therapeutic performance of the nanocomposites. Other studies on employing Fe-MOFs to coat UCNPs have been reported [54,69–71,81,92,93], confirmed the advantages of combing UCNPs with Fe-MOFs in constructing multifunctional nanocomposites for cancer theranostics applications.

3.2. Metallic oxides

Fe_3O_4 was introduced into Fe-MOF structures to amplify catalytic characteristics, while also remained the features deriving from the flexible crystalline and porous architectures [147,148]. Pu *et al.* reported the IR-780 FLI agent decorated, GSH-depleting Fe_3O_4@MIL-100 (IFM) nanocomposite for catalytic tumor therapy [38]. The nanocomposite integrated the function of self-supplement of tumoral H_2O_2 using β-lapachone for CDT and localized hyperthermia under near infrared light irradiation (Fig. 9a). As depicted in the TEM image in Fig. 9b, IFM showed a nearly spherical core-shell structure. To evaluate the potential of IFM for tumors-specific PAI, 4T1-bearing mice were intratumorally injected with IFM. As shown in Fig. 9c, a peak in PA signal was observed after 24 h injection of IFM, providing spatiotemporal information at tumor sites essential for precise cancer therapy. According to the findings of PAI, the strongest FL signal in tumor region was seen after 24 h the injection (Fig. 9d). These results confirmed that both PAI and FLI could clearly distinguish the tumor sites from the surrounding background tissues. Therefore, the photothermal conversion *in vivo* was conducted under 808 nm laser (1.0 W/cm^2) irradiation for after 24 h injection of IFM, and the tumor temperatures were measured using a thermal imager. Among all groups, the highest temperature of 58.1 °C was obtained in the IFM plus 808 nm laser group after 5 min irradiation (Fig. 9e). *In vivo* antitumor assays were conducted to evaluate the combined CDT and PTT effects of the IFM. Fig. 9f confirmed that combination of IFM, β-lapachone and 808 nm laser irradiation produced the best therapeutic effect. Within 14 days of treatment, the weight of mice in all groups showed an incremental tendency, indicating that the sample had good biosafety (Fig. 9g).

3.3. MOF-on-MOF

Owing to distinct topology and adjustable pore structure of MOFs, constructing composite MOF materials is a creative concept that expands the functionality of single MOF materials. A special structure is referred as MOF-on-MOF hybrid, which has the ability to integrate the properties of two MOFs [149–151]. MOF-on-MOF hybrids have been used in the field of antitumor due to their synergistic effects of components [152,153], and dual enzyme-mimic performance enhancing the function of cascade catalytic [88,154,155]. For example, Du *et al.* designed bimetallic core-shell Fe-MOF-on-Tb-MOF nanoplatform with the method of MOF-on-MOF, employing it as transducer materials for aptasensors [88]. The aptasensors demonstrated excellent sensing capabilities for monitoring a tumor marker of ovarian cancer: carbohydrate anti-

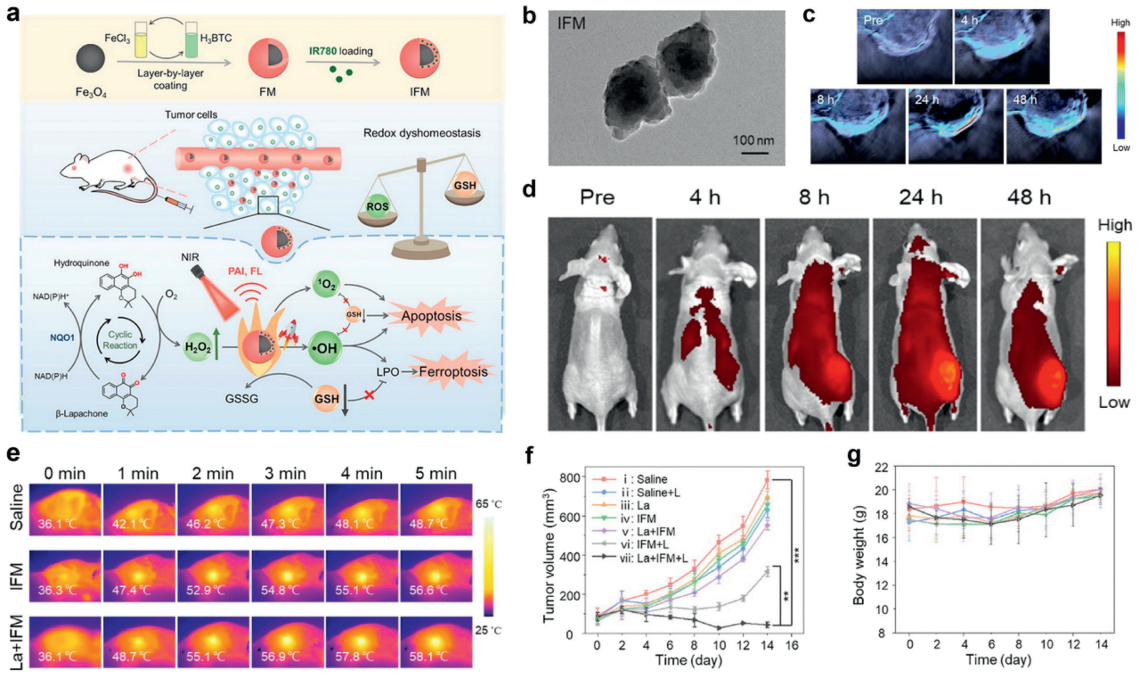

Fig. 9. (a) Illustration of IR780-loaded IFM for photo-enhanced upcycling H_2O_2 into highly cytotoxic $^{\bullet}OH$ for intense nanocatalytic tumor therapy. (b) TEM images of IFM. (c) *In vivo* PAI of 4T1 tumors at various time points before and after intravenous injection of IFM. (d) Time-dependent *in vivo* FLI post intravenous administration of IFM. (e) Infrared thermal images. (f) Tumor volume changes during treatment. (g) Tumor weights of different groups after 14 days of treatment. Reproduced with permission [38]. Copyright 2022, Elsevier Ltd.

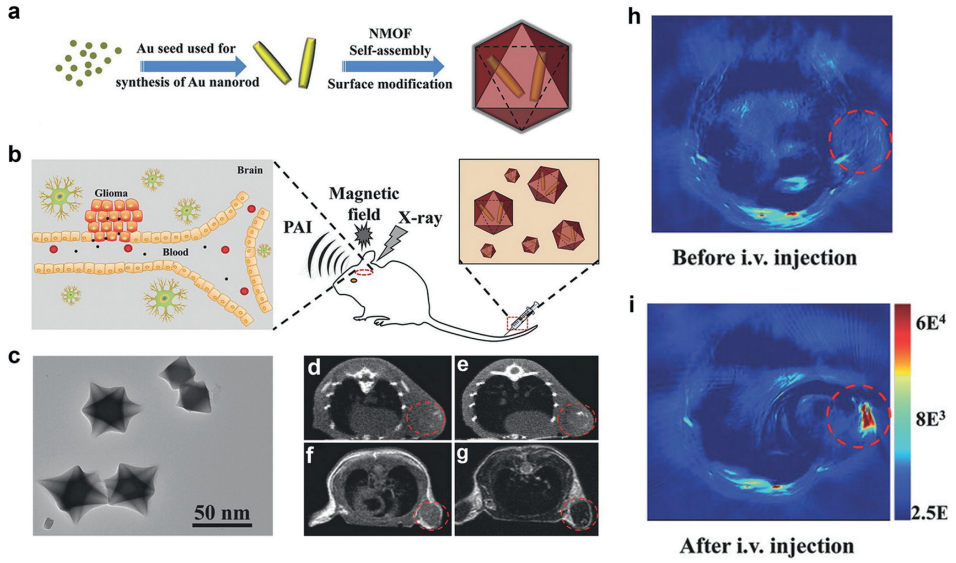

Fig. 10. (a) Schematic illustration of the synthesis of Au@MIL-88(Fe) nanostars. (b) Application to multimodality imaging-based tumor diagnosis. (c) TEM image of Au@MIL-88(A) nanoparticles. (d, e) CTI of mice before and 12 h after intravenous injection with Au@MIL-88(Fe). (f, g) T_2-weighted MRI of mice before and after intravenous injection with Au@MIL-88(Fe). (h, i) *In vivo* PAI of tumors in mice before and 12 h after intravenous injection with Au@MIL-88(Fe). Reproduced with permission [55]. Copyright 2016, Wiley-VCH Verlag GmbH & Co. KGaA, Weinheim.

gen (CA) 125 and living MCF-7 cells. Bimetallic TbFe-MOF hybrid structure combined strong anchoring to the Fe-MOFs aptamer strand with FLI activity of Tb-MOF, which showed higher stability for forming G-quadruplex between aptamer and CA125 to achieve good sensing performance compared with other aptasensors [156].

3.4. Au NPs

Au NPs exhibit multiple enzyme-like performance, making them widely applicable in the field of biological catalysis [157,158]. Researchers are increasingly interested in employing Au NPs to mimic natural enzymes due to their demonstrated catalytic efficiency when supported by zeolites and mesoporous materials [159]. Similarly, Fe-MOFs offer crucial benefits as platforms for incorporating Au NPs, producing the effect of cascade catalysis [160,161]. Tian *et al.* constructed the Au@MIL-88A(Fe) nanostars for multimodality diagnoses of glioma, including computed tomography imaging (CTI), PAI and MRI (Figs. 10a and b) [55]. TEM image showed that the morphology of high monodispersity and homogeneity for Au@MIL-88A(Fe) (Fig. 10c). The *in vivo* imaging ability of the nanostars were studied on U87 MG-orthotopic-tumor-

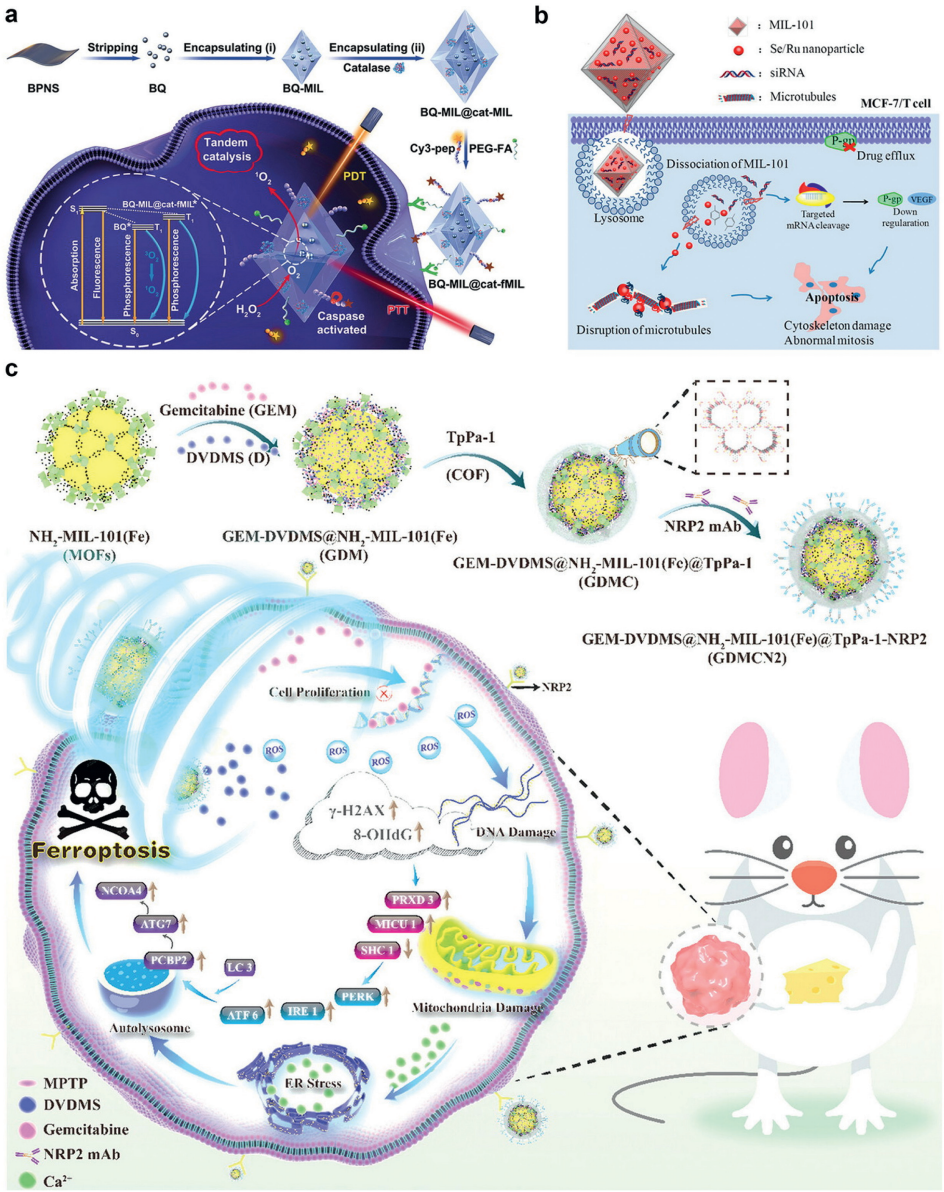

Fig. 11. (a) Stepwise assembly of BQ and CAT in MOF layers and its application as tandem catalyst for enhanced therapy against hypoxic tumor cells. Reproduced with permission [82]. Copyright 2019, Wiley-VCH Verlag GmbH &Co. KGaA, Weinheim. (b) Mechanism of the reversal of drug resistance and induced apoptosis by the disruption of microtubule in MCF-7/T (Taxol-Resistance) cancer cells. Reproduced with permission [85]. Copyright 2017, American Chemical Society. (c) SDT of NRP2 mAb-guided MOFs@COF targeted disruption of mitochondrial and ER homeostasis to induce autophagy-dependent ferroptosis. Reproduced with permission [37]. Copyright 2023, Wiley-VCH GmbH.

bearing mice. Figs. 10d–g displayed images that 24 h after intravenous injection with Au@MIL-88(Fe), and the white dots in tumor region were observed for 8 h post-injection (Fig. 10e), confirming the good computed tomography imaging contrast ability of Au@MIL-88(Fe) *in vivo* as well as sufficient accumulation of Au@MIL-88(Fe) occurred in tumor site. T_2-weighted images were obtained from U87MG-bearing mice to assay the MRI nature of Au@MIL-88(Fe). As depicted in Fig. 10g, T_2-weighted signals were observed in the tumor region 8 h postinjection with Au@MIL-88(Fe). Additionally, the *in vivo* PAI capability of the Au@MIL-88(Fe) was examined using the tumor bearing mice. Compared to the weak signal before 12 h intravenous injection (Fig. 10h), a clear contrast was observed, revealing the good PAI nature of Au@MIL-88(Fe) (Fig. 10i). Overall, the trimodal imaging capabilities of Au@MIL-88(Fe) inspire the design of nanoplatforms with enhanced spatial and temporal resolution for glioma imaging.

3.5. Other heterostructure into Fe-MOFs

3.5.1. QDs

Black phosphorus QDs (BQ) displays optical properties due to the quantum confinement and edge effects, which have nature for generation of $^1O_2$ and good photothermal conversion efficiency for PTT [162,163]. Lei *et al.* developed that the BQ and CAT were precisely encapsulated into the inner and outer layers of Fe-MOF (BQ-MIL@cat-MIL), respectively, through a stepwise *in situ* growth method [82]. The BQ-MIL@cat-MIL can be regarded as a tandem catalyst to generate O_2 by catalyzing H_2O_2 to compensate hypoxic condition in TME for enhancing PDT. The extra oxygen supply could alleviate the hypoxia condition and improve the generation of $^1O_2$ efficiency in TME. As a result, the apoptotic efficiency of the system was 8.7-fold higher compared to that without CAT (Fig. 11a). In summary, the stepwise growth of the Fe-MOF hybrid

created two confined regions that allowed for precise assembly of individual components, resulting in enhanced activities and establishing a rational tandem for their performance.

3.5.2. Selenium/ruthenium (Se/Ru) NPs

Se/Ru NPs are known for antitumor activity and low toxicity, drawing extending focus by researchers in recent years [164,165]. For example, Liu *et al.* reported that Se/Ru NPs modified MIL-101(Fe), which could deliver pooled small interfering RNAs (siRNAs) to MCF-7/T (Taxol-resistant) cells to disrupt microtubule dynamics and silence genes associated with multidrug resistance to improve the effectiveness of therapy (Fig. 11b) [85]. In conclusion, the unsaturated metal sites of MIL-101(Fe) can chelate with cysteine, facilitating the reduction of selenite and ruthenium to form Se/Ru@MIL-101 NPs. The high porosity of MIL-101(Fe) and the modification with Se/Ru NPs resulted in Se/Ru@MIL-101 enhancing the protection of siRNAs against nuclease degradation. This modification also increased cellular uptake for siRNAs, leading to enhanced cytotoxicity through the induction of apoptosis.

3.5.3. COF

COFs, a new class of organic crystalline polymers, are renowned for the adjustable porosity and well-defined molecular shape. COFs have been reported to exhibit remarkable biodegradability, resulting in drug release responsive to TME [166]. For example, Luo *et al.* designed a Fe-MOF nanocage encased in a COF and further modified with the pancreatic cancer-specific antibody, NRP2 and monoclonal antibody (GDMCN2), to generate multiple ROS while released chemotherapeutics *via* under US irradiation to realize SDT (Fig. 11c). Owing to the function of Fe-MOFs induce LPO accumulation and GPX4 decrease resulting in ferroptosis, GDMCN2 nanocage have prospect to combine apoptosis with ferroptosis for clinical elimination pancreatic cancer in future.

4. Conclusion and outlook

In conclusion, we have summarized the recent advances in engineered Fe-MOFs nanoplatforms, which are endowed multifunctional theranostics modes *via* integrating inorganic NPs or organic molecules into the single framework. Additionally, the EPR effects of Fe-MOFs provide a reliable mechanism to facilitate catalytic therapy at tumor sites. In this review, the nanoplatforms are categorized based on various Fe-MOFs to guide future research for efficient combined theranostics.

Nevertheless, there are certain challenges as follows that require further attention to achieve optimal clinical translation of Fe-MOFs. (1) The synthesis of multifunctional Fe-MOFs-based nanoplatforms often involves laborious procedures during functionalization processes, which greatly restricts their large-scale applicability. Indeed, building Fe-MOFs-based nanoplatforms with straightforward structures and versatile function is crucial for cancer treatment. (2) While numerous works have studied the toxicity of Fe-MOFs-based nanoplatforms *in vitro* and *in vivo*, most of the investigations have focused on their short-term toxicity, often neglecting the assessment of acute and long-term toxicity. (3) Extensive research has been conducted on the stability of Fe-MOFs-based nanoplatforms in PBS and simulated physiological environments. However, it is important to consider the complexities of natural physiological environments when assessing the stability of Fe-MOFs-based nanoplatforms. (4) While Fe-MOFs-based nanoplatforms have demonstrated potent anticancer effects in mice and other animal models, more research is needed to understand their impact on humans. (5) The ferroptosis properties of Fe-MOFs-based nanoplatforms have emerged as a promising mechanism for inducing apoptosis in tumor cells [2,50]. (6) The development of metal doping in Fe-MOFs can enhance their structural stability, as well as modulate their pore structure and specific surface area, thereby improving their performance in loading chemotherapy drugs within complex TME [167–177]. (7) Regulating Fe-MOFs-mediated catalytic therapy for anticancer research through metal doping is a promising approach [47,178–181].

In the future, the design of anticancer nanoplatforms can focus on combining ferroptosis and imaging-mediated CDT, PDT, SDT, PTT as well as immunotherapy. Besides, exploring additional metal cations to assess their effects on the structure and function of Fe-MOFs, which may result in the development of Fe-MOFs with improved performance for specific applications Noteworthy, natural forestry-derived polyphenols can be selected as organic ligands for constructing Fe-MOFs, offering a cost-effective and environmentally friendly alternative to many traditional Fe-MOFs ligands. Benefiting to the abundant active groups of natural polyphenols, metal-oxygen coordination bonds exhibit robust forces that lie between typical non-covalent interactions and covalent bonds, thereby imparting kinetic stability to metal chelates [182,183]. Other natural polyphenols such as tannic acid [95], epigallocatechin-3 gallate [96], artemisinin [97], gossypol [98], anthocyanins [99], ellagic acid [100] and dopamine [101] also show significant anticancer effects in cancer treatment after coordinating with various ion ions.

Consequently, the circulation time of the developed natural polyphenol-based Fe-MOFs in the bloodstream can be extended, thereby enhancing treatment efficiency by promoting tumor accumulation. Significantly, the high-valued application of natural products in cancer therapy can be realized.

Overall, despite facing numerous obstacles for cancer theranostics, the tremendous advancements in Fe-MOFs-based nanoplatforms have facilitated their further practical applications. Thoughtful design of multifunctional Fe-MOFs-based nanoplatforms will continuously provide assistant to cancer theranostics. In this regard, based on published studies, Fe-MOFs-based nanoplatforms, represent a feasible option to achieve the worthy objective of efficient cancer theranostics and improve the quality of human life in future.

Declaration of competing interest

The authors declare that they have no known competing financial interests or personal relationships that could have appeared to influence the work reported in this paper.

CRediT authorship contribution statement

Yunlong Li: Writing – review & editing, Writing – original draft, Investigation. **Xinyu Zhang:** Visualization. **Shuang Liu:** Writing – review & editing. **Chunsheng Li:** Methodology. **Qiang Wang:** Writing – review & editing. **Jin Ye:** Supervision. **Yong Lu:** Conceptualization. **Jiating Xu:** Writing – review & editing, Methodology, Funding acquisition.

Acknowledgments

Financial support from National Key Research and Development Program of China (No. 2022YFD2200602), 111 Project (No. B20088), National Natural Science Foundation of China (Nos. 52202345 and 31930076), and the Heilongjiang Touyan Innovation Team Program (Tree Genetics and Breeding Innovation Team) are greatly acknowledged.

Supplementary materials

Supplementary material associated with this article can be found, in the online version, at doi:10.1016/j.cclet.2024.110501.

References

[1] Q.H. Zhou, D. Dutta, Y.F. Cao, ACS Nano 17 (2023) 9374–9387.
[2] J.H. Du, M.T. Zhou, Q. Chen, et al., Adv. Funct. Mater. 33 (2023) 2215244.
[3] J.N. Huang, N. Li, C.M. Zhang, Z.W. Meng, ACS Appl. Mater. Interfaces 10 (2018) 38729–38738.
[4] Q.Y. Zheng, X.M. Liu, S. Gao, et al., Small 19 (2023) 2207687.
[5] M. Liu, Y.T. Ning, M. Ren, et al., Small 19 (2023) 2303876.
[6] X.Y. Li, B.B. Ding, J. Li, et al., Nano Res. 17 (2024) 6342–6352.
[7] L. Yang, S.M. Dong, S.L. Gai, et al., Nano-Micro Lett. 16 (2023) 28.
[8] M.F. Wang, P.A. Ma, J. Lin, Chin. Chem. Lett. 34 (2023) 108300.
[9] Y.A. Zeng, D.H. Liao, X.Y. Kong, et al., Colloid Surf. B: Biointerfaces 232 (2023) 113612.
[10] Z.Y. Luo, Y. Sheng, C.Y. Jiang, et al., Dalton Trans. 52 (2023) 17601–17622.
[11] Q.Y. Huang, Y.N. Zeng, Y.Z. Qiu, et al., Dyes Pigm. 222 (2024) 111865.
[12] G.J. Tan, S.Y. Wang, J.L. Yu, et al., Food Chem. 430 (2024) 136934.
[13] M.M. Li, Z.X. Zhang, Y.M. Yu, et al., Mater. Adv. 4 (2023) 5050–5093.
[14] Z.Q. Lin, D.H. Liao, C.Y. Jiang, et al., RSC Med. Chem. 14 (2023) 1914–1933.
[15] H.P. Yang, D.H. Liao, Z.D. Cai, et al., RSC Med. Chem. 14 (2023) 2473–2495.
[16] J.T. Liu, J. Huang, L. Zhang, J.P. Lei, Chem. Soc. Rev. 50 (2021) 1188–1218.
[17] Y.J. Deng, M.L. Guo, L.Y. Zhou, et al., Biomater. Sci. 12 (2024) 3725–3744.
[18] S.D. Huang, H.Q. Lu, J. Chen, et al., J. Mat. Chem. B 12 (2024) 6532–6549.
[19] C.Y. Jiang, L.Y. Zhou, W.B. Hu, et al., Mater. Today Chem. 36 (2024) 101964.
[20] Y. Song, L.X. Zhang, Y.Q. Wang, et al., Adv. Mater. 35 (2023) 2210895.
[21] N. Raeisi-Kheirabadi, A. Nezamzadeh-Ejhieh, H. Aghaei, ACS Omega 7 (2022) 31413–31423.
[22] N. Raeisi-Kheirabadi, A. Nezamzadeh-Ejhieh, ChemistrySelect 7 (2022) e202203788.
[23] S.L. Yang, L. Peng, S. Bulut, W.L. Queen, Chem. Eur. J. 25 (2018) 2161–2178.
[24] S.M.J. Rogge, A. Bavykina, J. Hajek, et al., Chem. Soc. Rev. 46 (2017) 3134–3184.
[25] R. Medishetty, J.K. Zareba, D. Mayer, et al., Chem. Soc. Rev. 46 (2017) 4976–5004.
[26] S.Z. Wang, C.M. McGuirk, A. d'Aquino, et al., Adv. Mater. 30 (2018) 1800202.
[27] X.Y. Lou, Y.P. Li, Y.W. Yang, Biotechnol. J. 14 (2018) 1800354.
[28] Z. Li, N. Song, Y.W. Yang, Matter 1 (2019) 345–368.
[29] C.S. Li, J. Ye, X. Yang, et al., ACS Nano 16 (2022) 18143–18156.
[30] X.Y. Zhang, P. Wang, Y. Zhang, et al., ACS Appl. Mater. Interfaces 15 (2023) 3348–3356.
[31] M. Yang, Y.N. Zhou, Y.N. Cao, et al., Appl. Mater. Today 20 (2020) 100692.
[32] W.H. Kong, L.L. Wang, Y. Zhao, et al., Nano Today 38 (2021) 101126.
[33] Y.D. Pan, R. Abazari, B. Tahir, et al., Coord. Chem. Rev. 499 (2024) 215538.
[34] H.S. Wang, Coord. Chem. Rev. 349 (2017) 139–155.
[35] F. Liu, L. Lin, Y. Zhang, et al., Adv. Mater. 31 (2019) 1902885.
[36] R.Q. Liu, J.N. Yang, Y.Q. Du, et al., Adv. Mater. 36 (2023) 2310522.
[37] Z.Y. Zhao, Y.J. Wu, X.C. Liang, et al., Adv. Sci. 10 (2023) 2303872.
[38] J.E. Cun, Y. Pan, Z.Z. Zhang, et al., Biomaterials 287 (2022) 121687.
[39] M. Lismont, L. Dreesen, S. Wuttke, Adv. Funct. Mater. 27 (2017) 1606314.
[40] S.M. Li, L.F. Tan, X.W. Meng, Adv. Funct. Mater. 30 (2020) 1908924.
[41] S. Mallakpour, E. Nikkhoo, C.M. Hussain, Coord. Chem. Rev. 451 (2022) 214262.
[42] M.K. Sarangi, L. Patel, G. Rath, et al., Chin. Chem. Lett. 35 (2024) 109381.
[43] Y. Song, X.R. Xu, Z. Wang, Y.J. Zhao, Adv. Healthc. Mater. 13 (2024) 2303533.
[44] A. Hashemzadeh, G.P.C. Drummen, A. Avan, et al., J. Mat. Chem. B 9 (2021) 3967–3982.
[45] B. Liu, M. Jiang, D.Z. Zhu, et al., Chem. Eng. J. 428 (2022) 131118.
[46] W.Y. Li, Z.H. Liang, P.L. Wang, Q. Ma, Biosens. Bioelectron. 249 (2024) 116008.
[47] Y.L. Li, C.S. Li, S. Liu, et al., J. Colloid Interface Sci. 676 (2024) 974–988.
[48] C.L. Hu, J.Z. Wang, S.N. Liu, et al., ACS Appl. Mater. Interfaces 13 (2021) 4825–4834.
[49] C.L. Hao, L. Huang, H.Y. Zhang, et al., Adv. Funct. Mater. 34 (2023) 2312795.
[50] B.W. Yang, L. Ding, H.L. Yao, et al., Adv. Mater. 32 (2020) 1907152.
[51] B. Du, M. Zheng, H.Z. Ma, et al., J. Nanobiotechnol. 20 (2022) 209.
[52] T. Wang, C.C. Wang, Y. Wang, et al., Adv. Funct. Mater. 34 (2024) 2400791.
[53] B.Y. Wu, J.T. Fu, Y.X. Zhou, et al., Acta Pharm. Sin. B 10 (2020) 2198–2211.
[54] X.Y. Chen, Y. Chen, C.C. Wang, et al., Angew. Chem. Int. Ed. 60 (2021) 21905–21910.
[55] W.T. Shang, C.T. Zeng, Y. Du, et al., Adv. Mater. 29 (2016) 1604381.
[56] X.Y. Wan, L.Q. Song, W. Pan, et al., ACS Nano 14 (2020) 11017–11028.
[57] W. Cai, H.Y. Gao, C.C. Chu, et al., ACS Appl. Mater. Interfaces 9 (2017) 2040–2051.
[58] R. Huang, W.R. Liu, Q.H. Zhang, et al., ACS Appl. Mater. Interfaces 15 (2023) 3781–3790.
[59] Y.D. Zhu, S.P. Chen, H. Zhao, et al., ACS Appl. Mater. Interfaces 8 (2016) 34209–34217.
[60] H.S. Liu, C.N. Xu, M. Meng, et al., Acta Biomater. 144 (2022) 132–141.
[61] T. Xue, C.N. Xu, Y. Wang, et al., Biomater. Sci. 7 (2019) 4615–4623.
[62] J.Z. Yao, Y. Liu, J.W. Wang, et al., Biomaterials 195 (2019) 51–62.
[63] H. Yu, Y. Cheng, C. Wen, et al., Biomaterials 280 (2022) 121308.
[64] Y. Zhang, L. Lin, L. Liu, et al., Biomaterials 216 (2019) 119255.
[65] H. Yu, H.Y. Zhao, Y.J. Zhang, et al., Chem. Eng. J. 472 (2023) 144690.
[66] S. Sheng, F. Liu, L. Lin, et al., J. Control. Release 328 (2020) 631–639.
[67] W.S. Ni, K. Jiang, Q.M. Ke, et al., J. Mater. Sci. Technol. 141 (2023) 11–20.
[68] S.L. Luo, Y.T. Zhao, K.W. Pan, et al., Biomater. Sci. 9 (2021) 6772–6786.
[69] X.X. Wang, J.T. Xu, D. Yang, et al., Chem. Eng. J. 354 (2018) 1141–1152.
[70] D. Yang, J.T. Xu, G.X. Yang, et al., Chem. Eng. J. 344 (2018) 363–374.
[71] W.E. Bao, M. Liu, J.Q. Meng, et al., Nat. Commun. 12 (2021) 6399.
[72] Z.J. Fan, H.X. Liu, Y.H. Xue, et al., Bioact. Mater. 6 (2021) 312–325.
[73] L.Y. Wang, D. Lu, M.F. Huo, H.X. Xu, Adv. Funct. Mater. 32 (2022) 2106332.
[74] H.B. Ji, C.R. Kim, C.H. Min, et al., Bioeng. Transl. Med. 8 (2023) 1–14.
[75] H.S. Wu, D.H. Gu, S.J. Xia, et al., Biomater. Sci. 9 (2021) 1020–1033.
[76] P.H. Wu, P.F. Cheng, W. Kaveevivitchai, T.H. Chen, Colloid Surf. B: Biointerfaces 225 (2023) 113264.
[77] F. Gao, C. Xue, J.H. Dong, et al., Small 20 (2023) 2307736.
[78] B.L. Li, Z.J. Wu, X.T. Xu, et al., Inorg. Chem. Front. 11 (2024) 4439–4448.
[79] Z.M. Mo, X.Y. Pan, X.L. Pan, et al., J. Mat. Chem. B 10 (2022) 8760–8770.
[80] P.P. Yang, J. Tao, F.F. Chen, et al., Small 17 (2021) 2005865.
[81] Y.T. Li, J.L. Tang, L.C. He, et al., Adv. Mater. 27 (2015) 4075–4080.
[82] J.T. Liu, T.R. Liu, P. Du, et al., Angew. Chem. Int. Ed. 58 (2019) 7808–7812.
[83] X.Y. Ma, X.L. Ren, X.D. Guo, et al., Biomaterials 214 (2019) 119223.
[84] J.M. Li, J. Dai, L. Zhao, et al., Adv. Funct. Mater. 33 (2023) 2303254.
[85] Q.C. Chen, M. Xu, W.J. Zheng, et al., ACS Appl. Mater. Interfaces 9 (2017) 6712–6724.
[86] W.T. Zhang, C. Liu, Z.W. Liu, et al., ACS Nano 16 (2022) 20975–20984.
[87] Y. Jiang, H. Lu, L.L. Lei, et al., Colloid Surf. B: Biointerfaces 240 (2024) 113981.
[88] M.H. Wang, M.Y. Hu, Z.Z. Li, et al., Biosens. Bioelectron. 142 (2019) 111536.
[89] L. Liang, L.L. Yang, W.J. Wang, et al., Adv. Mater. 33 (2021) 2102271.
[90] Z.W. Chen, Y.J. Sun, J.W. Wang, et al., ACS Nano 17 (2023) 9003–9013.
[91] Z. Wang, B. Liu, Q.Q. Sun, et al., ACS Nano 15 (2021) 12342–12357.
[92] L.C. He, Q.Q. Ni, J. Mu, et al., J. Am. Chem. Soc. 142 (2020) 6822–6832.
[93] T. Jia, J.R. Du, J.N. Yang, et al., Adv. Funct. Mater. 34 (2024) 2307816.
[94] P.S. Zhang, Y. Hou, J.F. Zeng, et al., Angew. Chem. Int. Ed. 58 (2019) 11088–11096.
[95] T. Liu, W.L. Liu, M.K. Zhang, et al., ACS Nano 12 (2018) 12181–12192.
[96] Z.G. Ren, S.C. Sun, R.R. Sun, et al., Adv. Mater. 32 (2019) 1906024.
[97] J. Chen, X.B. Wang, Y. Zhang, et al., Biomaterials 266 (2021) 120457.
[98] Z. Zhang, W. Sang, L.S. Xie, et al., Angew. Chem. Int. Ed. 60 (2020) 1967–1975.
[99] C.N. Xu, Y.B. Wang, H.Y. Yu, et al., ACS Nano 12 (2018) 8255–8265.
[100] G.Z. Zhao, H.H. Wu, R.L. Feng, et al., ACS Appl. Mater. Interfaces 10 (2018) 3295–3304.
[101] G. Chen, Y.Y. Yang, Q. Xu, et al., Nano Lett. 20 (2020) 8141–8150.
[102] M.E. Medina, Y. Dumont, J.M. Grenèchec, F. Millange, Chem. Commun. 46 (2010) 7987–7989.
[103] M.X. Wu, J. Gao, F. Wang, et al., Small 14 (2018) 1704440.
[104] D.W. Feng, Z.Y. Gu, J.R. Li, et al., Angew. Chem. Int. Ed. 51 (2012) 10307–10310.
[105] K.C. Wang, D.W. Feng, T.F. Liu, et al., J. Am. Chem. Soc. 136 (2014) 13983–13986.
[106] D.L. Meng, C.H. Chen, J.D. Yi, et al., Research 2019 (2019) 1768595.
[107] X.X. Yang, X. Xu, M.F. Wang, et al., J. Nanobiotechnol. 20 (2022) 230.
[108] Z.D. Liu, S.A. Liu, B. Liu, et al., Chin. Chem. Lett. 35 (2024) 109626.
[109] W.S. Ni, L. Zhang, H.R. Zhang, et al., Inorg. Chem. 61 (2022) 3281–3287.
[110] S. Bauer, C. Serre, T. Devic, et al., Inorg. Chem. 47 (2008) 7568–7576.
[111] C. MellotDraznieks, C. Serre, S. Surblé, et al., J. Am. Chem. Soc. 127 (2005) 16273–16278.
[112] S.N. Kim, C.G. Park, B.K. Huh, et al., Acta Biomater. 79 (2018) 344–353.
[113] Y.L. Liu, X.J. Zhao, X.X. Yang, Y.F. Li, Analyst 138 (2013) 4526–4531.
[114] Y.J. Zhang, S.W. Jin, R.L. Liu, et al., Environ. Res. 250 (2024) 118499.
[115] B.R. Stockwell, J.P.F. Angeli, H. Bayir, et al., Cell 171 (2017) 273–285.
[116] G. Férey, C. Serre, C. Mellot-Draznieks, et al., Angew. Chem. Int. Ed. 43 (2004) 6296–6301.
[117] D.K. Wang, M.T. Wang, Z.H. Li, ACS Catal. 5 (2015) 6852–6857.
[118] S. Sheng, L. Lin, F. Liu, et al., Chem. Mat. 34 (2022) 8664–8674.
[119] N. Yodsin, K. Sriphumrat, P. Mano, et al., Microporous Mesoporous Mat. 343 (2022) 112187.
[120] S.H. Shen, Y.S. Wu, K. Li, et al., Biomaterials 154 (2018) 197–212.
[121] P. Serra-Crespo, E.V. Ramos-Fernandez, J. Gascon, F. Kapteijn, Chem. Mat. 23 (2011) 2565–2572.
[122] F.K. Shieh, S.C. Wang, C.I. Yen, et al., J. Am. Chem. Soc. 137 (2015) 4276–4279.
[123] S. Peng, B.L. Bie, Y.Z.S. Sun, et al., Nat. Commun. 9 (2018) 1293.
[124] P. Horcajada, T. Chalati, C. Serre, et al., Nat. Mater. 9 (2009) 172–178.
[125] M.M. Sun, L.L. Wang, Y. Zhuo, et al., Small 20 (2024) 2309593.
[126] T. Araya, M.K. Jia, J. Yang, et al., Appl. Catal. B: Environ. 203 (2017) 768–777.
[127] D.D. Zhang, Nature 626 (2024) 269–270.
[128] Z. Wang, B. Liu, Q.Q. Sun, et al., ACS Appl. Mater. Interfaces 12 (2020) 17254–17267.
[129] J. Zhu, C.C. Chu, D.S. Li, et al., Adv. Funct. Mater. 29 (2019) 1904056.
[130] J.Y. Yu, Z.H. Guo, J.C. Yan, et al., Adv. Sci. 10 (2023) 2206957.
[131] Z.Y. Ye, Y. Bao, Z.F. Chen, et al., Coord. Chem. Rev. 504 (2024) 215654.
[132] B.S. Tian, S.H. Liu, C.H. Yu, et al., Adv. Funct. Mater. 33 (2023) 202300818.
[133] Y.J. Bao, H.F. Ru, Y.F. Wang, et al., Adv. Funct. Mater. 34 (2024) 2314611.
[134] Y.J. Jiang, T.Y. Chen, J.L. Chen, et al., Adv. Mater. 36 (2024) 2306910.
[135] H.B. Peng, X.C. Zhang, P. Yang, et al., Bioact. Mater. 19 (2023) 1–11.
[136] W.J. Chen, D. Gupta, M.Y. Yang, et al., Small 19 (2023) 2303403.
[137] Y.J. Ai, H. Sun, Z.X. Gao, et al., Adv. Funct. Mater. 31 (2021) 2103581.
[138] S.Y. Luo, Y. Wang, S.H. Shen, et al., Adv. Funct. Mater. 31 (2021) 2100954.
[139] Y.R. Wang, J.A. Zhou, L. Yuan, et al., Small 19 (2023) 2206657.
[140] L. An, C.L. Yan, X.L. Mu, et al., ACS Appl. Mater. Interfaces 10 (2018) 28483–28493.
[141] Y.F. Shi, G. Zhang, C. Xiang, et al., Adv. Mater. 36 (2024) 2305162.
[142] G.H. Yang, R.Y. Fan, J.Q. Yang, et al., Biomaterials 302 (2023) 122347.
[143] S. Liu, X.P. Xu, J. Ye, et al., Chem. Eng. J. 456 (2023) 140892.
[144] J.F. Zeng, M. Cheng, Y. Wang, et al., Adv. Healthc. Mater. 5 (2016) 772–780.
[145] C.C. Liu, C.C. Li, S. Jiang, et al., Nanoscale Adv. 4 (2022) 173–181.

[146] F.Y. Liu, X.X. He, H.D. Chen, et al., Nat. Commun. 6 (2015) 8003.
[147] A.R. Chowdhuri, T. Singh, S.K. Ghosh, S.K. Sahu, ACS Appl. Mater. Interfaces 8 (2016) 16573–16583.
[148] S. Sene, M.T. Marcos-Almaraz, N. Menguy, et al., Chem 3 (2017) 303–322.
[149] S.Y. Yin, G.S. Song, Y. Yang, et al., Adv. Funct. Mater. 29 (2019) 1901417.
[150] Y.C. Chai, S.H. Chen, Y. Chen, et al., J. Am. Chem. Soc. 146 (2023) 263–273.
[151] L.J. Mao, J.J. Qian, Small 20 (2024) 2308732.
[152] Y.N. Jin, X.C. Mi, J.L. Qian, et al., ACS Appl. Mater. Interfaces 14 (2022) 48285–48295.
[153] Y.K. Zhao, Y. Zhang, X.G. Cao, et al., Chem. Eng. J. 465 (2023) 143000.
[154] N. Zhou, F.F. Su, C.P. Guo, et al., Biosens. Bioelectron. 123 (2019) 51–58.
[155] J.Y. Zhao, Y.Y. Long, C.J. He, et al., Chem. Eng. J. 479 (2024) 147513.
[156] Z.H. Zhang, H.F. Ji, Y.P. Song, et al., Biosens. Bioelectron. 94 (2017) 358–364.
[157] J.N. Li, W.Q. Liu, X.C. Wu, X.F. Gao, Biomaterials 48 (2015) 37–44.
[158] D.W. Jiang, D.L. Ni, Z.T. Rosenkrans, et al., Chem. Soc. Rev. 48 (2019) 3683–3704.
[159] V. Lykourinou, Y. Chen, X.S. Wang, et al., J. Am. Chem. Soc. 133 (2011) 10382–10385.
[160] Y.H. Hu, H.J. Cheng, X.Z. Zhao, et al., ACS Nano 11 (2017) 5558–5566.
[161] Y.L. Liu, W.L. Fu, C.M. Li, et al., Anal. Chim. Acta 861 (2015) 55–61.
[162] H. Wang, S.L. Jiang, W. Shao, et al., J. Am. Chem. Soc. 140 (2018) 3474–3480.
[163] T. Guo, Y. Wu, Y. Lin, et al., Small 14 (2017) 1702815.
[164] Y.F. Wang, J.L. Wang, H. Hao, et al., ACS Nano 10 (2016) 9927–9937.
[165] W.L. Kwong, K.Y. Lam, C.N. Lok, et al., Angew. Chem. Int. Ed. 55 (2016) 13524–13528.
[166] S. Bhunia, K.A. Deo, A.K. Gaharwar, Adv. Funct. Mater. 30 (2020) 2002046.
[167] X.R. Guo, L.Y. Zhou, X.Z. Liu, et al., Colloid Surf. B: Biointerfaces 229 (2023) 113455.
[168] S.H. Zhou, L. Lu, D. Liu, et al., CrystEngComm 23 (2021) 8043–8052.
[169] J.Y. Chen, F. Cheng, D.W. Luo, et al., Dalton Trans. 51 (2022) 14817–14832.
[170] J.Y. Chen, Z.X. Zhang, J.X. Ma, et al., Dalton Trans. 52 (2023) 6226–6238.
[171] C.Y. Rao, D.H. Liao, Y. Pan, et al., Expert Opin. Drug Deliv. 19 (2022) 1183–1202.
[172] Y.N. Zeng, G.H. Xu, X.Y. Kong, et al., Int. J. Pharm. 627 (2022) 122228.
[173] R. Sheikhsamany, A. Nezamzadeh-Ejhieh, R. Ensandoost, B. Kakavandi, J. Mol. Liq. 403 (2024) 124850.
[174] W.F. Zhang, G.M. Ye, D.H. Liao, et al., Molecules 27 (2022) 7166.
[175] W.P. Chen, M. Liu, H.P. Yang, et al., Pharmaceutics 15 (2023) 1323.
[176] D.H. Liao, J.F. Huang, C.Y. Jiang, et al., Pharmaceutics 15 (2023) 2071.
[177] S. Lal, P. Singh, A. Singhal, et al., RSC Adv. 14 (2024) 3413–3446.
[178] Q.Z. Wang, X.W. Zhu, X.W. Meng, H.S. Zhong, Acta Biomater. 172 (2023) 382–394.
[179] K.R. Chen, A.W. Zhou, X.Y. Zhou, et al., Sci. Adv. 10 (2024) eadk3201.
[180] Z.Z. Feng, G. Chen, M. Zhong, et al., Biomaterials 302 (2023) 122333.
[181] Q.Y. Shi, Y. Zhao, M.H. Liu, et al., Small 20 (2023) 2309366.
[182] X.L. Liao, Y.S. Zheng, Z.G. Lin, et al., Chem. Eng. J. 400 (2020) 125882.
[183] H.F. Sun, R. Chang, Q.L. Zou, et al., Small 15 (2019) 1905326.